

A mechanistic study of the effect of temperature on crack propagation in Alloy 600 under PWR primary water conditions

Zhao Shen, Sergio Lozano-Perez

University of Oxford, Department of Materials, Parks Road, OX1 3PH Oxford, UK

Abstract

The stress corrosion cracking (SCC) of three Alloy 600 has been studied in the simulated primary water of pressurized water reactor at 290°C, 320°C, 340°C, and 360°C. A clear correlation between the experiment temperature and the crack growth rate was found that the crack growth rate increased monotonously with the experiment temperature used in this study. In order to understand the temperature dependence of crack growth rate, high-resolution characterization was used to study the crack tips (CTs) prepared from Alloy 600 tested at 320°C, 340°C, and 360°C. After an initial observation of the SCC crack paths on the polished cross-section surfaces via optical microscopy, a plan-view site-specific sample preparation technique via a focused ion beam has been used to prepare transmission electron microscopy (TEM) samples containing active CTs. The CTs obtained from different temperatures were detailedly analyzed through high-resolution analytical TEM to reveal the CT morphology and chemistry, which enable the study of a thermally activated diffusion-based mechanism operating during the SCC propagation. A high-resolution transmission Kikuchi diffraction was used to investigate a mechanical respond-based mechanism in the SCC propagation through quantifying the size and extent of plastic deformation around the CTs. Results obtained in this study shows that the thermally activated diffusion along the grain boundary increased with the temperature while the plastic deformation around the CT was very low and nearly independent with the temperature, indicating the thermally activated diffusion-based mechanism was the adominant one during the SCC propagation, which correspond well with the temperature dependence of crack growth rate of Alloy 600.

Key words: stress corrosion cracking; temperature dependence; crack growth rate; Alloy 600; transmission electron microscopy; transmission Kikuchi diffraction

1. Introduction

Alloy 600 has been widely used as components in the primary circuit of pressurized water reactors (PWRs) such as steam generator tubing and reactor pressure boundary nozzle assemblies [1, 2]. However, this material was reported to be very susceptible to stress corrosion cracking (SCC) in the high-temperature water environment, which has caused many accidents in the commercial PWRs. To keep the safely running of PWR during its whole service lifetime, it is necessary to be able to predict the remaining lifetime and mitigate the cracking behavior. After several decades of study, a considerable number of factors have been revealed that affect the SCC susceptibility, including material compositions, pre-exist cold-work, temperature, water chemistry, etc. [3-6]. Among them, temperature is one of the most important factors that can significantly influence the crack growth rate (CGR).

The temperature dependence of SCC growth of austenitic alloys, such as 316 steel, Alloy 800, Alloy 690, and Alloy 600, has been detailedly studied via autoclave testing by Arioka et al. [4]. The authors found that the dependences of temperature on the CGR of these materials were different. The existence of peak temperature in the CGR was observed in almost all these materials except for the Alloy 600, showing that the CGR of these materials was suppressed at higher temperatures. While the CGR of the Alloy 600 increased monotonously with

temperatures. Although the different dependences of temperature on the CGR have been reveal by the authors, the underlying reasons are still missing.

In a recent literature [7], high resolution characterization techniques such as analytical transmission electron microscopy (ATEM) and transmission Kikuchi diffraction (TKD) were used to mechanistically study the suppression effect on the CGR at higher temperatures in the 20% cold-worked of 316 steel. The samples used in this literature were provided by Arioka [4]. After the study, the authors found that the existence of peak temperature was the result of the combined effects of two rate-controlling factors: thermally activated elemental diffusion and mechanical response to external stress and internal strain.

In the current study, the principle aim is to mechanistically understand the dependence of temperature on the CGR of Alloy 600. Three Alloy 600 specimens after autoclave testing at 320°C, 340°C, and 360°C were provided by Arioka (for details see [4]). Nine TEM samples containing CTs (CTs) from three specimens were characterized by high-resolution ATEM and TKD. By comparing the key features obtained from the characterization, such as the length of Cr-depletion zone ahead of CTs, the plastic deformation intensity around CTs, and Cr-rich oxide distribution around the CTs, the monotonous increase of CGR of Alloy 600 with temperature shall be explained.

2. Experimental

2.1 Material and SCC test

The materials used in this study were Alloy MA600 tested under simulated primary water conditions of PWR at 320°C, 340°C, and 360°C, provided by the laboratory of INSS (Japan). The chemical compositions and microstructures of this alloy are listed in Table 1 and Fig. 1. Prior to autoclave testing, the specimen was mill-annealed in air at 930°C followed by water quenching to obtain chromium carbides at grain boundaries since chromium precipitates were reported to be beneficial in improving SCC resistance [8, 9]. Cold work in austenitic alloys was shown to be detrimental to SCC, however, it is inevitable during manufacturing and installation [4-6]. Therefore, to simulate the real working condition of Alloy 600, the specimen was cold-worked prior to the autoclave testing. Cold work in the specimen was produced through uni-directional rolling at room temperature to a thickness reduction of 20%, which was also referred to as 20% cold work. The SCC test was conducted at the laboratory of INSS (Japan) using a pre-cracked 1/2 compact tension specimen in the T-L direction (crack growth direction parallel to the rolling direction) in an autoclave under a constant load of 30 MPam^{1/2}. More details can be found in reference [4]. Before destructive examination of the fracture surface, one piece of cross-section sample was cut out from the 1/2 compact tension sample after autoclave testing. These cross-sectioned samples were then ground with SiC paper, followed by polishing with 1-μm diamond suspension. A mirror-finished surface was obtained after 25 minutes of final treatment with colloidal silica in order to clearly show the SCC CTs. The parameters about the CGRs and the number of CTs used in this study are listed in Table 2.

Table 1 Chemical content of Alloy 600 used in this study (wt%)

Alloy	C	Cr	Fe	Si	Mn	P	S	Cu	Ni
600	0.06	16.02	6.94	0.33	0.35	0.006	<0.001	0.03	76.26

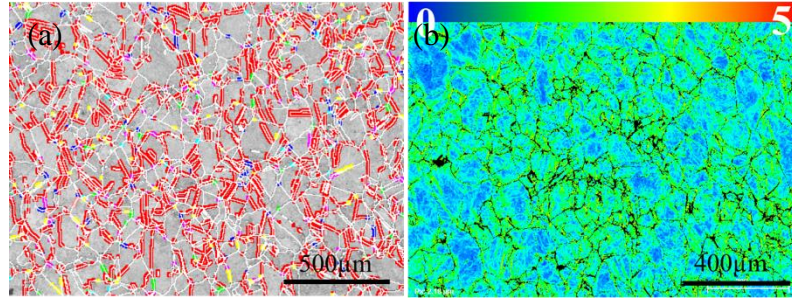


Fig. 1. Microstructure of MA600 Alloy obtained from electron backscattered diffraction (step size = 4 μm) analysis. (a) distribution of grain boundaries (twin boundary in red, random high angle grain boundary in white); (b) Kernel misorientation map.

Table 2 Alloy 600 bulk specimen data: test duration; total length of crack path; calculated CGR; total number of SCC CTs found in sample; number of SCC CTs prepared as TEM lamella via FIB.

Specimen	Test temperature (°C)	Test duration (h)	Total crack length (mm)	CGR (mm/s)	Number of active CT
Alloy 600	320	1000	2.0	5.6×10^{-7}	3
	340	765	4.4	1.6×10^{-6}	4
	360	355.2	6.1	4.8×10^{-6}	2

2.2 Methodology

2.2.1 Site-specific sample preparation with FIB

Sample preparation was reported to be critical for the data quality obtained from TEM and TKD analysis [10, 11]. For example, electron energy loss spectroscopy (EELS) requires the sample thickness to be around 50 nm while the TKD analysis needs sample without evident bending. To study specific CT, FIB plan-view sample preparation technique was adopted in this study. A single beam FEI FIB200 equipped with a static micromanipulator was used for trenching and in-situ lift-out. A dual beam Zeiss NVision 40 FIB-SEM was subsequently used for thinning sample to a thickness less than 50nm. Since FIB milling could introduce significant damage on the sample surface, final low energy cleaning (5 kV, 250 pA) with FIB should be performed on both sides of the thin foil after a conventional milling to minimize the damage. More details can be found in reference [12].

2.2.2 ATEM analysis

Since the nature of small features around CT area, the traditional relatively low-resolution techniques, such as secondary electron microscopy (SEM), are not enough to provide atomic-level resolution data. Therefore, in this study, ATEM is adopted to approach information in atomic scale. Once CT samples were well prepared, TEM analysis was performed with a JEOL 2100 (operating voltage 200 kV) equipped with an Oxford energy-dispersive X-ray (EDX) detector system for preliminary imaging and selective area diffraction. The following high-resolution analysis, including STEM and EELS, was conducted with a JEOL ARM200F (cold-field emission gun) operating at 200 kV and equipped with a Quantum Gatan image filter (GIF) spectrometer. The core-loss spectra of EELS were quantitatively processed by a Gatan Digital Micrograph to extract individual maps for all selected elements. Then drift-compensation on core-loss spectra was achieved via comparing with the positions of low-loss spectra using the software of Hyperspy 1.1 (open source) to correct statistical errors and noise.

2.2.3 TKD analysis

TKD analysis was performed using a Zeiss Crossbeam 540 FEG-SEM equipped with Oxford Instrument EBSD detector system. To obtain optimum working condition, the sample was 20° pre-tilted with respect to horizontal, and the working distance was set to 5 mm. Meantime, an accelerating voltage of 20 kV and a probe current of 1.5 nA was used. The step sizes were set as 10 nm. The data was subsequently post-processed by the software of Channel 5. Image quality maps, misorientation (MO) maps, and inverse pole figure (z-axis) (IPFZ) maps were exported automatically by the software, and MO line profiles were extracted manually.

3. Results

According to results reported in literature [13-15], the mechanism controlling SCC in Alloy 600 exposed to primary water of PWR should be an internal oxidation along grain boundaries. The results from the ATEM analysis in this study also support this mechanism, which will be discussed later. The internal oxidation mechanism was first proposed by Scott et al. [16]. Since the SCC occurred in Alloy 600 was intergranular, the authors believed that the failure of grain boundary was mainly due to the faster grain boundary oxidation rate than the crack propagation rate. Once the grain boundary was oxidized, it tended to be very susceptible to cracking. As a result, the grain boundary oxidation rate is the dominant factor affecting the CGR. Literature shows that there are mainly three factors influencing the grain boundary oxidation rate and then affecting the CGR: 1) the thermally activated elemental diffusion ability along grain boundaries; 2) the protective ability of the Cr-rich oxide formed in grain boundaries; 3) the extent of plastic deformation in grain boundaries [4, 7, 8, 13-16]. In this study, these three factors were identified by ATEM and TKD first, and then were used to study the temperature dependence of CGR. Among them, the length of Cr-depletion zone ahead of the Cr-rich oxide was used to describe the thermally activated elemental diffusion ability along the grain boundary; the oxygen diffusion length ahead of the Cr-rich oxide was used to describe the protective ability of Cr-rich oxide; the intensity of lattice rotation around the CT was used to describe the extent of plastic deformation. Since the exposure time can change the chemistry around the CTs, to maximally reduce the influence of different exposure time, only active CTs were used in this study because they were still propagating and almost exposed to PWR water for similar time when they were taken out from the autoclave. This precondition is indispensable to directly compare the features observed around different CTs because different exposure time can significantly change both structure and chemistry around CTs, which makes the results are not comparable. It is necessary to note that although the CTs were taken out from the deepest region, but it does not necessarily mean that the CTs were exposed to the water for completely a same time. Therefore, differences caused by the different exposure time still existed. Furthermore, results in literature [8, 9] shows that grain boundary carbides can change the SCC propagation but the effect of carbide on SCC will not be discussed in this work. As a result, in order to maximally eliminate the influences introduced by the grain boundary carbides, the active CTs used in this study are those not arrested by the carbides when the specimens were taken out from the autoclave.

3.1 ATEM characterization

Six active CTs were observed at the deepest region of SCC cracks developed in the Alloy 600 tested at 320°C. However, three of the CTs were arrested by grain boundary carbides. Therefore, only three active CTs could be used. The elemental distribution around these three active CTs were analyzed by electron energy loss spectroscopy (EELS). One of the typical EELS analysis result is presented in Fig. 2a. Since the high angle annular dark-field (HAADF) image is very sensitive to the atomic density, it is available to distinguish the regions of the crack and the oxygen diffusion zone ahead of CTs. The existence of oxygen diffusion zone ahead of CT is one of the typical characteristics of internal oxidation mechanism [17]. Previous studies showed that the Cr-rich oxide was always existed just ahead of CTs in austenitic alloys, which was critical to the protection of grain boundary from further oxidation [7, 8, 14, 18, 19]. However, Cr-rich oxide was not observed just ahead of all CTs tested at 320°C but at

the tips of oxygen diffusion zone, as shown in Cr-map of Fig. 2a. The existence of preferential oxidation of Cr and expulsion of Ni further proved that the mechanism operating in the SCC propagation was internal oxidation. The length of Cr-depletion zone ahead of Cr-rich oxide was around 95 nm. Since the oxygen diffusion was completely restrained by the Cr-rich oxide, the oxygen diffusion length ahead of Cr-rich oxide was zero. The chemical compositions of the Cr-rich oxide were 29% O, 18% Cr, 3% Fe and 49% Ni.

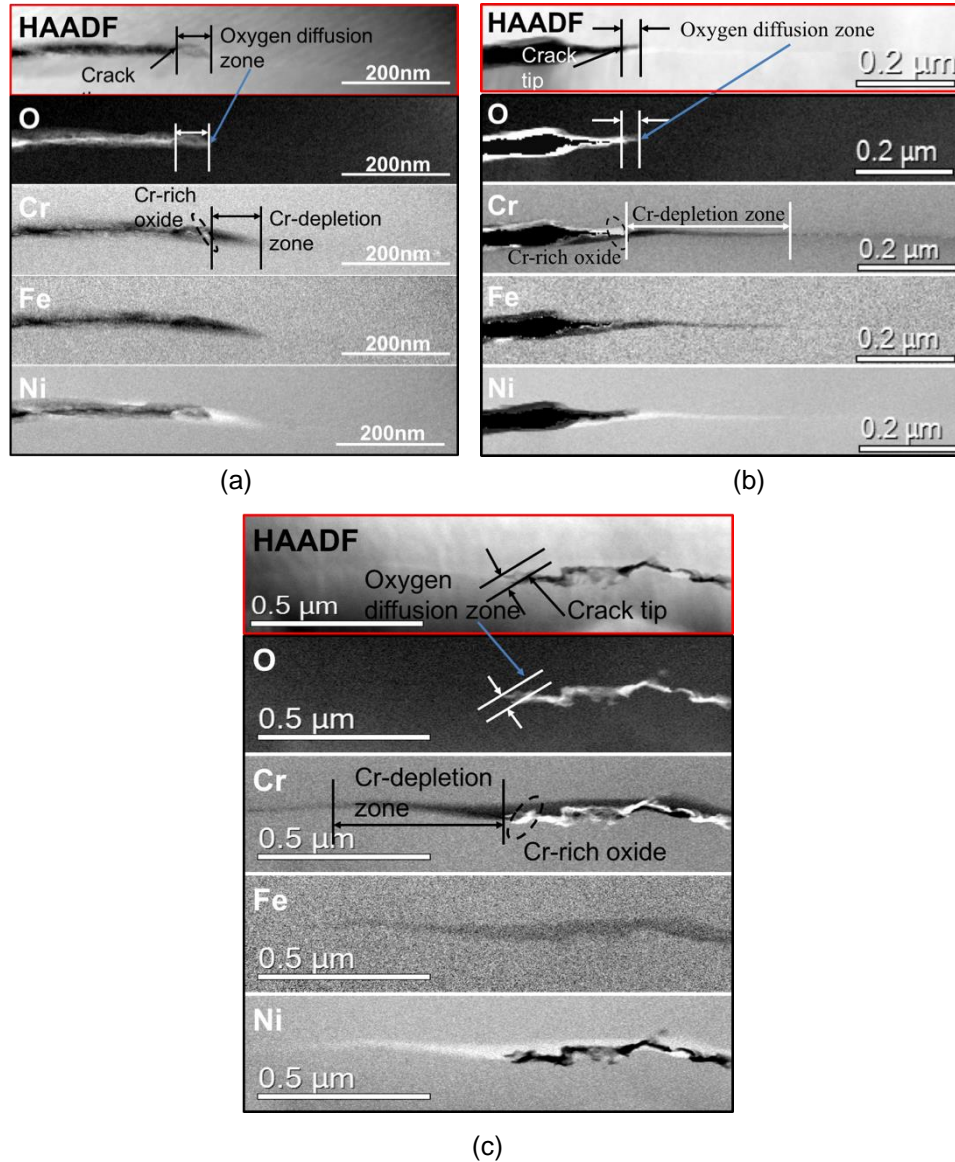


Fig. 2. STEM images and EELS elemental maps of grain boundary diffusion ahead of the CT in high-temperature samples; top: HAADF images, bottom: EELS elemental O K edge and Cr/Fe/Ni L edge maps; a) Alloy 600 tested at 320°C, CT Cr-rich oxide contains 28% O, 18% Cr, 3% Fe and 49% Ni; b) Alloy 600 tested at 340°C, CT Cr-rich oxide contains 57% O, 26% Cr, 4% Fe and 8% Ni; c) Alloy 600 tested at 360°C, CT Cr-rich oxide contains 55% O, 33% Cr, 2% Fe and 9% Ni.

Seven active CTs were prepared from the deepest region of SCC cracks developed in the Alloy 600 tested at 340°C, while three of them were affected by the grain boundary carbides and only four of them were eligible to be used in this study. One of the typical CTs tested at 340°C after ATEM analysis was shown in Fig. 2b. The Cr-rich oxide was observed just ahead of the CT. The chemical compositions of this Cr-rich oxide was 57% O, 26% Cr, 4% Fe and 8% Ni. However, the oxygen diffusion along the grain boundary was not completely prevented by

this Cr-rich oxide. The length of the oxygen diffusion zone was around 75 nm. The Cr-depletion zone ahead of the oxygen diffusion zone was also observed and the length of this zone was around 320 nm.

There were six active CTs at the deepest region of SCC cracks while only three of them were not influenced by the grain boundary carbides at 360°C. The ATEM analysis results obtained from a typical CT was presented in Fig. 2c. The Cr-rich oxide was observed ahead of the CT, consisting of 55% O, 33% Cr, 2% Fe and 9% Ni. The oxygen diffusion was not thoroughly restricted by the Cr-rich oxide, leading to the formation of oxygen diffusion zone just ahead of this Cr-rich oxide. The length of the oxygen diffusion zone was only 74 nm. However, the length Cr-depletion zone ahead of the oxygen diffusion zone reached 585 nm.

In order to accurately present the results obtained from ATEM, the length of Cr-depletion zone ahead of Cr-rich oxide, the length of oxygen diffusion ahead of Cr-rich oxide, and the compositions of Cr-rich oxide were averaged for each temperature. Results are summarized in Table 3. Although the relative errors in the quantitative EELS measurements was better than 10%, the procedure of averaging the results from all crack tips from a given temperature will introduce statistical errors (standard deviation).

Table 3 Average Cr-depletion length, oxygen diffusion length ahead of Cr-rich oxide, and Cr-rich oxide composition for the different samples. The parameters displayed were measured and averaged from all crack tips from a given temperature.

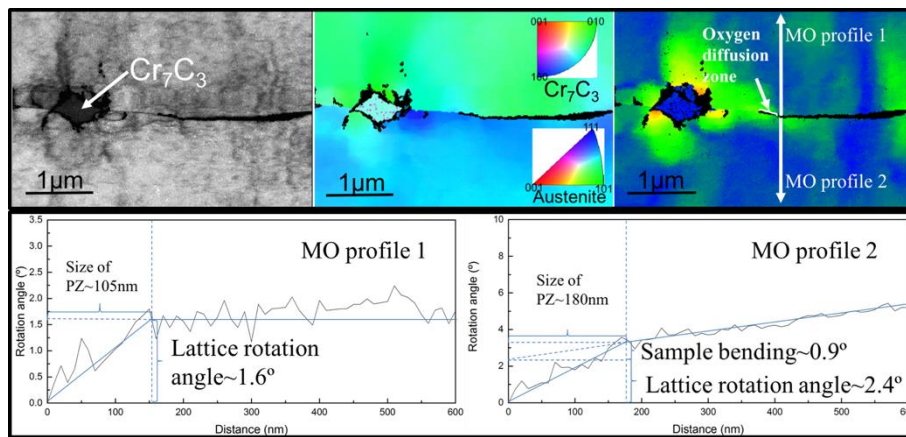
Materials	Cr-depletion length (nm)	Oxygen diffusion length (nm)	Cr-rich oxide compositions			
			O (at.%)	Cr (at.%)	Fe (at.%)	Ni (at.%)
Alloy 600-320°C	121 ± 53	0	29 ± 8	19 ± 2	3 ± 2	48 ± 9
Alloy 600-340°C	325 ± 67	72 ± 43	54 ± 9	32 ± 3	4 ± 2	8 ± 3
Alloy 600-360°C	556 ± 82	81 ± 56	55 ± 6	29 ± 3	3 ± 2	9 ± 4

3.2 TKD characterization

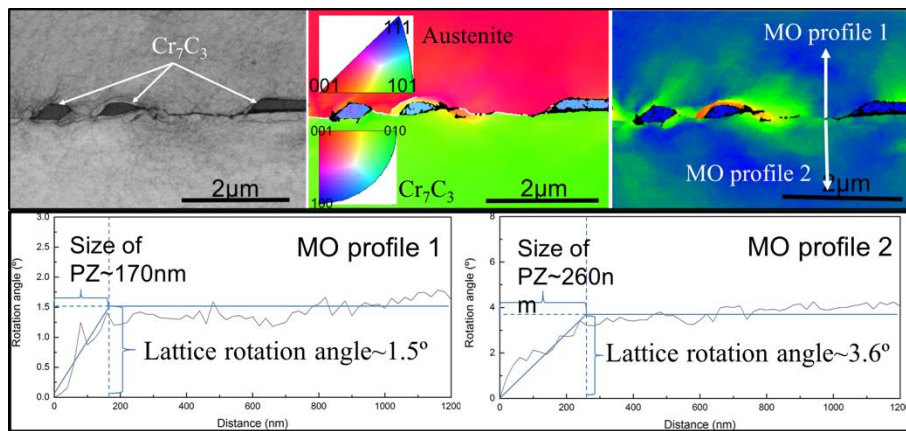
Taking into account the impacts of yield strength [6] and plastic deformation [4, 5, 20] on the SCC susceptibility, the mechanical response to the prior internal stress and externally applied loading during the SCC testing was thought to be another critical factor affecting the SCC resistance. TKD was first utilized by Meisnar et al. [7, 10] in the study of SCC, trying to understand the relationship between SCC growth and crystallographic features around the CTs. The authors have proved that the MO line profiles extracted from the TKD average MO map are applicable in describing the size and extent of plastic zone around CT after comparing with data obtained from high-resolution Kernel average MO map that was acquired using the cross-correlation-based analysis of the TKD patterns. Therefore, to locally measure the plastic deformation around CTs, all TEM samples containing CTs were studied via TKD after the ATEM analysis. The step sizes for all samples were as low as 10nm. The high-quality TEM sample preparation with FIB made the hit rates of all TKD measurements be better than 90%. The zero resolution pixels in all TKD maps were labeled using a black color.

Three active CTs prepared from Alloy 600 tested at 320°C were analyzed by TKD. TKD maps acquired from one of the active CTs are presented in Fig. 3a. The high-resolution of TKD technique enabled the identification of the positions of the grain boundary and crack from TKD maps. It is necessary to mention that there was a portion of grain boundary region just ahead of the CT that was also not indexed. This region should be ODZ observed in section 3.1 since the material in this zone was no longer austenitic phase after severe oxidation. The length of this region was similar to the length of ODZ observed in ATEM, which further supports this hypothesis.

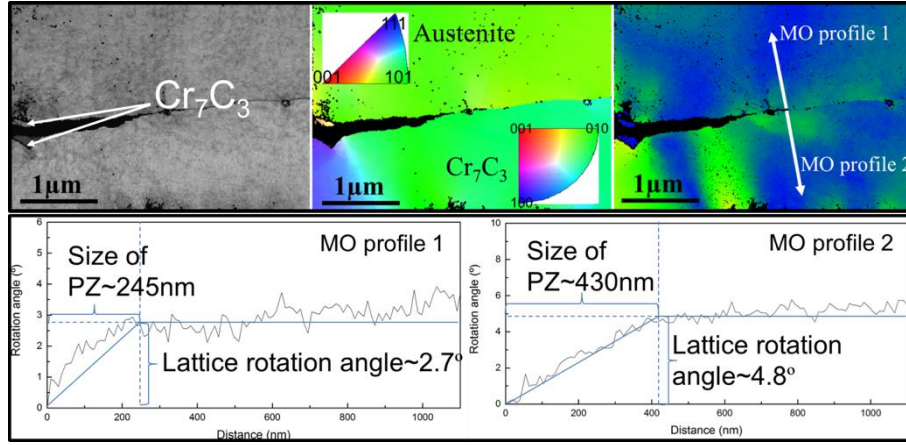
A grain boundary precipitate was observed in Fig. 3a. This precipitate was identified as Cr_7C_3 by the TKD patterns. To measure the plastic deformation, two MO profiles were extracted from the CT outwards into the matrix, as shown in Fig. 3a. Further observation of MO profiles reveals a locally elevated lattice rotation adjacent to the CT. Meisnar et al. [7, 10] believed that this very localized lattice rotation were the results of the prior cold-work and later external-load. Since the thickness of the samples used in this study was only around 50 nm, some of the samples was bended during the sample thinning. As a result, to measure the lattice rotation angle caused by the plastic deformation, it is necessary to subtract the lattice rotation angle caused by the sample bending. Details about how to calculate the size and extent of plastic deformation can be found in references [7, 10]. The region of plastic deformation around the CTs was named as plastic zone (PZ) in this work. The MO profile 1 (see Fig. 3a) shows that the size of PZ in the top grain was around 105 nm, and the lattice rotation angles was $1.6 \pm 0.7^\circ$. The MO profile 2 (see Fig. 3a) reveals that the size of PZ in the bottom grain was around 180 nm and the lattice rotation angle was $3.3 \pm 0.6^\circ$. However, the lattice rotation angle measured in the bottom grain was not purely caused by the plastic deformation because there were two slopes in the MO profile 2. The presence of the second slope indicated that this region was bent. To obtain the lattice rotation angle that was purely caused by the plastic deformation, the sample bending introduced lattice rotation should be subtracted. Since the lattice rotation angle caused by the sample bending in the PZ was determined to be $0.9 \pm 0.6^\circ$, the lattice rotation angle induced by the plastic deformation was calculated to be $2.4 \pm 0.6^\circ$. It worth noting that plastic deformation around the grain boundary carbide is very high, but its effect on crack propagation is not clear. That is why the CTs used in this study were those not arrested by the carbides.



(a)



(b)



(c)

Fig. 3. TKD maps and MO profiles extracted around CTs in high-temperature samples; top: TKD pattern quality map (left), IPFZ map (middle), and average MO map (right); bottom: MO profiles; a) Alloy 600 tested at 320°C, PZ size~105 nm/lattice rotation angle~ $1.6 \pm 0.7^\circ$ (MO profile 1), PZ size~180 nm/lattice rotation angle~ $2.4 \pm 0.6^\circ$ (MO profile 2); b) Alloy 600 tested at 340°C, PZ size~170 nm/lattice rotation angle~ $1.5 \pm 0.5^\circ$ (MO profile 1), PZ size~260 nm/lattice rotation angle~ $3.6 \pm 0.7^\circ$ (MO profile 2); c) Alloy 600 tested at 360°C, PZ size~245 nm/lattice rotation angle~ $2.7 \pm 1.1^\circ$ (MO profile 1), PZ size~430 nm/lattice rotation angle~ $4.8 \pm 0.9^\circ$ (MO profile 2).

Four active CTs prepared from Alloy 600 tested at 340°C were all tested by TKD. One of the typical results is presented in Fig. 3b. Three grain boundary carbides were observed in this sample and there were all identified as Cr_7C_3 . Preferential plastic deformation was also revealed to surround these carbides. The plastic deformation around the CT was measured by the MO profiles. MO profile 1 (see Fig. 3b) shows that size of PZ and lattice rotation angle caused by the plastic deformation in the top grain were $1.5 \pm 0.5^\circ$ and 170 nm, respectively. MO profile 2 (see Fig. 3b) shows that the size of PZ and lattice rotation angle caused by the plastic deformation in the bottom grain were $3.6 \pm 0.7^\circ$ and 260 nm, respectively.

Two active CTs prepared from Alloy 600 tested at 360°C were all tested by TKD. The TKD results obtained from one CT were shown in Fig. 3c. MO profiles were conducted to measure the plastic deformation around CT. MO profile 1 reveals that the size of PZ and lattice rotation angle in the top grain were 245 nm and $2.7 \pm 1.1^\circ$, respectively. MO profile 2 shows that the size of PZ and lattice rotation angle in the top grain were 430 nm and $4.8 \pm 0.9^\circ$, respectively.

The results obtained from TKD were averaged for each temperature, as shown in Table 4. The plastic deformation intensity was used to describe the temperature dependence of plastic deformation around CTs in this study. The plastic deformation intensity was defined as follow:

$$\text{Dislocation density} = \text{Lattice rotation angle} / \text{PZ size} \quad (1)$$

Once the PZ size and lattice rotation angle were measured, the dislocation density was calculated according to the equation (1) and the results were summarized in Table 4.

Table 4 Average PZ size, lattice rotation angle, and dislocation density for the different samples. The parameters displayed were calculated and averaged from all crack tips from a given temperature.

Materials	PZ size (nm)	Lattice rotation angle ($^\circ$)	Dislocation density ($^\circ/\text{nm} \times 100$)
Alloy 600-320°C	192 ± 83	2.3 ± 0.9	1.3 ± 0.7
Alloy 600-340°C	237 ± 77	2.55 ± 1.1	1.1 ± 0.7
Alloy 600-360°C	325 ± 91	3.74 ± 1.1	1.2 ± 0.8

4. Discussion

Arioka et al. [4] has discovered the existence of peak temperature in the study of temperature dependence of SCC in a series of austenitic alloys except the Alloy 600. Meisnar et al. [7] believed that the decline of CGR of 316 stainless steel at higher temperatures was because the mechanical response to external stress and internal strain played a more important role than the thermally activated diffusion at higher temperatures. If the mechanism proposed by Meisnar et al. [7] is correct, the monotonous increase of CGR with temperature of the Alloy 600 should be due to the dominant role of thermally activated diffusion at higher temperatures. From the results acquired in this study and elsewhere [8, 13-15], it is almost indisputable that the SCC mechanism operating in Alloy 600 is internal oxidation of grain boundaries. As it was mentioned in section 3, the CGR of Alloy 600 is mainly affected by three factors: 1) the thermally activated elemental diffusion ability along grain boundaries; 2) the protective ability of the Cr-rich oxide formed in grain boundaries; 3) the extent of plastic deformation in grain boundaries. The first two factors have been studied by ATEM, and the third factor has been revealed by TKD. As a result, in order to understand the temperature dependence of CGR, it is necessary to discuss the temperature dependence of these three factors separately.

4.1 The dependence of temperature on thermally activated diffusion

From a thermodynamic view, the internal oxidation is a diffusion-based process meaning that a higher diffusion rate at higher temperatures can lead to faster oxidation rate [21, 22]. Since the thermally activated diffusion could play a very important role in the SCC propagation, it is necessary to understand the temperature dependence of thermally activated diffusion. In this study, the process of diffusion includes the metallic diffusion (Fe, Cr, and Ni) and nonmetallic diffusion (oxygen). Compared with the diffusion rate of metallic elements, the oxygen diffusion rate was much higher. Therefore, the diffusion rate of metallic elements was the rate limit factor, and the effect of temperature on the oxygen diffusion rate will not be discussed. Furthermore, since the electrochemistry potential in the simulated PWR primary water was very low, the metallic Ni could not be oxidized. Considering the low content of Fe in the Alloy 600, the oxidation of the grain boundary mainly means the oxidation of metallic Cr. As a result, the thermally activated diffusion ability was described by the Cr diffusion ability along the grain boundary in this study. As mentioned in section 3.1, there was a Cr-depletion zone ahead of all CTs. The outward diffusion of Cr from the Cr-depletion zone was oxidized by the inward diffusion oxygen to form Cr-rich oxide. Therefore, the thermally activated diffusion ability of Cr at a specific temperature was described by the length of Cr-depletion zone ahead of the Cr-rich oxide (see Fig. 2). The effect of temperature on the thermally activated diffusion can be described by the different Cr-depletion length at different temperatures. In order to clearly show the relationship between the temperature dependence of thermally activated diffusion and CGR, the functions of the Cr-depletion length and the CGR versus the temperature were plotted in Fig. 3a. Since the two curves presented in Fig. 4a correlate very well with each other, the thermally activated diffusion should play a very important role in SCC propagation.

The role of thermally activated diffusion on the CGR can be not only quantified by the Cr-depletion length but also qualitatively described by the distribution of Cr-rich oxide around the CTs. Different from the formation of Cr-rich oxide at CTs at 340°C and 360°C, the Cr-rich oxide was not observed at the CTs at 320°C but at the tip of oxygen diffusion zone (see Fig. 2). This is mainly because the Cr diffusion rate at 320°C was not high enough to reach the CTs immediately and form Cr-rich oxide at CTs. As a result, the diffusion of oxygen along the grain boundaries will continue. Once the inward diffusion of oxygen meets the outward diffusion of Cr flux, the Cr oxide will form, which then restrains the further inward diffusion of oxygen. Except the different Cr-rich oxide positions, the content of Cr-rich oxide was much higher at higher temperatures, which can also support the conclusion that the Cr diffusion was accelerated at higher temperatures.

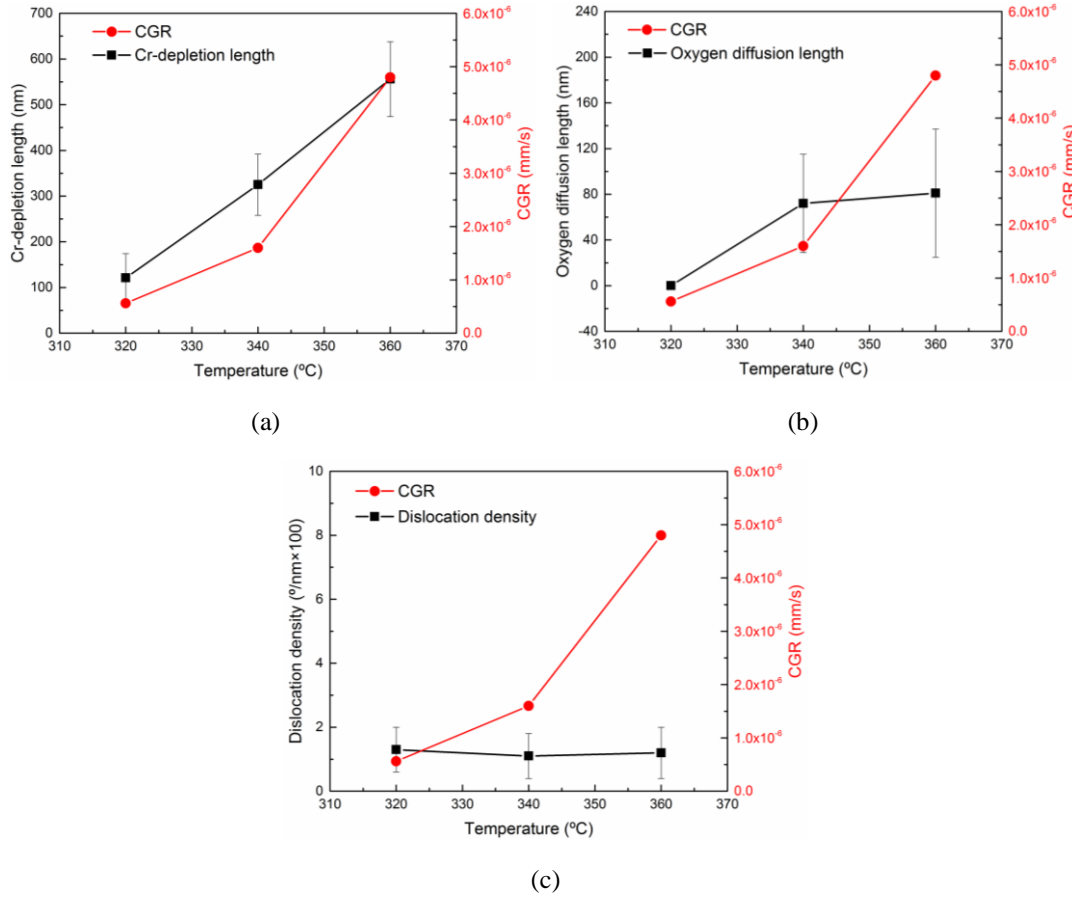


Fig. 4. a) Illustration of Cr-depletion length ahead of Cr-rich oxide at different temperatures; b) illustration of oxygen diffusion length ahead of Cr-rich oxide at different temperatures; c) illustration of dislocation density around CTs at different temperatures; Red line with square: temperature dependence of CGR for comparison.

4.2 The dependence of temperature on the protective ability of Cr-rich oxide

In the study of 316 stainless steel, Meisnar et al. [7] found that although the higher temperature could increase the oxidation rate in one way, the faster formation of Cr-rich oxide at CTs could decrease the further oxidation rate to some extent in another way. However, in this study although the content of the Cr-rich oxide and the content of Cr in the Cr-rich oxide was higher at higher temperatures, the protective ability of the Cr-rich oxide formed at 340°C and 360°C was even worse than the Cr-rich oxide formed at 320°C (see Table 3). As a result, the poor protective ability of Cr-rich oxide formed at higher temperatures should be another possible reason that contributed to the higher CGR at higher temperatures, as shown in Fig. 4b.

4.3 The dependence of temperature on plastic deformation

According to the results reported by Lozano-Perez et al. [5] and Terachi et al. [6], the plastic deformation in the material can strongly affect the SCC growth. Lozano-Perez found that the cold-work introduced plastic deformation in the 316 stainless steel can significantly assist the intergranular oxidation, which then influence the SCC susceptibility. Terachi showed that the CGR of stainless steels of 304 and 316 increased with the yield strength. The different yield strengths in these stainless steels were caused by the different degree of cold-work. Andresen et al. [23] and Shoji et al. [24] also observed similar phenomenon. They believed that the PZ size around a CT tend to be smaller in high yield strength alloys, which provided a higher strain gradient. Since the effective stress acted at the CT was higher, the CGR was increased. In the study of temperature dependence of CGR of 316 stainless steel, Meisnar et al. [7] found that the increase of temperature could remarkably reduce the plastic deformation around the CTs due to the decline of the yield strength. The higher extent of plastic deformation at

lower temperatures lead to the formation of higher content of defects around the CTs, which made the structure of the CTs tend to be more brittle and resulted in higher CGR at lower temperatures.

Similar to method used by Meisnar, the plastic deformation around the CTs of Alloy 600 tested at 320-360°C was measured by TKD (see section 3.2). Different from the results of 316 stainless steel [7], the extent of plastic deformation around the CTs was almost independent to the temperature, as shown in Table 4. Although the size of PZ at 320°C was smaller than those at 340°C and 360°C, the lattice rotation angle was also smaller. As a result, the effect of temperature on the dislocation density was negligible. To show the role of plastic deformation around CTs on the CGR, the effects of temperature on the dislocation density and CGR are compared in Fig. 4c. It is clear that there is almost no relationship between these two curves, indicating that the role of plastic deformation on the CGR of Alloy 600 is negligible.

The reason of different role of plastic deformation on CGR of Alloy 600 and 316 stainless steel [7] is still not clear. It might be because the CGR of Alloy 600 is much higher than 316 stainless steel when the experimental conditions are completely the same, which means the action time of the external stress loading at the CTs of Alloy 600 could be much longer than at the CTs of stainless steel. The longer action time could lead to higher extent of plastic deformation. Since the plastic deformation at the CTs of Alloy 600 is not as high as the CTs of 316 stainless steel, the effect of plastic deformation on the CGR of Alloy 600 is not as evident as 316 stainless steel. This explanation is very possible because the lattice rotation angles around the CTs of 316 stainless steel are much higher than Alloy 600.

4.4 The dependence of temperature on CGR of SCC

After the separately discussion of the effects of the three factors mentioned in section 3 on CGR of Alloy 600, it is clear that the CGR of Alloy 600 at a specific temperature was the result of the combination effect of these three factors. According to the results obtained in this study, the monotonous increase of the CGR of Alloy 600 with temperatures was mainly because the temperature remarkably increased the oxidation rate through accelerating the elemental diffusion. The reduce of the protective ability of the Cr-rich oxide ahead of CTs was another factor that contributed to the increase of CGR with temperatures. Although the PZ size around CTs increased with temperatures due the decline of yield strength, the dislocation density was almost independent to the temperature. As a result, the inhibition effect of this factor to CGR was very weak. It is necessary to point out that there might be more factors that could affect the CGR such as hydrogen embrittlement, but the characterization techniques used in this study cannot reveal the role of these factors. Therefore, they have not included in this study.

5. Conclusions

The temperature dependence of CGR in Alloy 600 exposed to simulated PWR primary water was investigated. There was no peak temperature in Alloy 600. The CGR increased monotonously with temperatures. Three factors, including 1) the thermally activated elemental diffusion ability along grain boundaries; 2) the protective ability of the Cr-rich oxide formed in grain boundaries; 3) the extent of plastic deformation in grain boundaries, were initially proposed to be very possible in resulting in the monotonous increase of CGR of Alloy 600 based on previous work. High-resolution ATEM and TKD were then used to detailedly study the effect of these three factors on the monotonous increase of CGR of Alloy 600. The results obtained in this work have been compared with the temperature dependence of CGR in 316 stainless steel.

ATEM analysis reveals that the factor of thermally activated diffusion played a dominant role in increasing CGR of Alloy 600 with temperatures. The decrease of the protective ability of Cr-rich oxide formed at 340°C and 360°C further accelerated the CGR. Although the thermally activated diffusion in 316 stainless steel was also found to be assisted by higher temperatures, the decrease of defect density around CTs with temperatures lead to the CT structure tend to be less brittle, which caused the decline of CGR at higher temperatures. The defect density

around CTs of Alloy 600 was not increased by higher temperatures and it was almost independent to temperatures. As a result, the CGR of Alloy 600 increased monotonously with temperatures, which is different to the temperature dependence of CGR of 316 stainless steel.

6. Acknowledgement

The authors would like to thank Koji Arioka (INSS) for providing the sample used in this study. Zhao Shen is also grateful to China Scholarship Council for providing financial support.

7. Reference

- [1] H. Coriou, L. Crall, Y. L. Gall, S. Vettier, 3rd Metallurgy Conf. on Corrosion, Saclay (Amsterdam, The Netherlands: North Holland Publishing Co., 1959), 1960, pp. 161-169.
- [2] W. Bamford, J. Hall, "Cracking of alloy 600 nozzles and welds in PWRs: review of cracking events and repair service experience.", in: Proceedings of the 12th Int'l Conf. on Environmental Degradation of Materials in Nuclear Power Systems – Water Reactor, Salt Lake City, UT, 2005, p. 959.
- [3] P.L. Andresen, M.M. Morra. Stress corrosion cracking of stainless steels and nickel alloys in high-temperature water. *Corrosion*, 64 (2008): 15-29.
- [4] K. Arioka, T. Yamada, T. Miyamoto, M. Aoki. Intergranular Stress Corrosion Cracking Growth Behavior of Ni-Cr-Fe Alloys in Pressurized Water Reactor Primary Water. *Corrosion*, 70(2014): 695-707.
- [5] S. Lozano-Perez, K. Kruska, I. Iyengar, T. Terachi, T. Yamada. The role of cold work and applied stress on surface oxidation of 304 stainless steel. *Corrosion Science*, 56(2012): 78-85.
- [6] T. Terachi, T. Yamada, T. Miyamoto, K. Arioka. SCC growth behaviors of austenitic stainless steels in simulated PWR primary water. *Journal of Nuclear Materials*, 426(2012): 59-70.
- [7] M. Meisnar, A. Vilalta-Clemente, M. Moody, K. Arioka, S. Lozano-Perez. A mechanistic study of the temperature dependence of the stress corrosion crack growth rate in SUS316 stainless steels exposed to PWR primary water. *Acta Materialia*, 114 (2016): 15-24.
- [8] M. Sennour, P. Laghoutaris, C. Guerre, R. Molins. Advanced TEM characterization of stress corrosion cracking of Alloy 600 in pressurized water reactor primary water environment. *Journal of Nuclear Materials*, 393(2009): 254-266.
- [9] H. Dugdale, D.E. Armstrong, E. Tarleton, S.G. Roberts, S. Lozano-Perez. How oxidized grain boundaries fail. *Acta Materialia*, 61(2013): 4707-4713.
- [10] M. Meisnar, A. Vilalta-Clemente, A. Gholinia, M. Moody, A.J. Wilkinson, N. Huin, S. Lozano-Perez. Using transmission Kikuchi diffraction to study intergranular stress corrosion cracking in type 316 stainless steels. *Micron*, 75(2015): 1-10.
- [11] R.R. Keller, R.H. Geiss. Transmission EBSD from 10 nm domains in a scanning electron microscope. *Journal of Microscopy*, 245(2012): 245-251.
- [12] S. Lozano-Perez. A guide on FIB preparation of samples containing stress corrosion crack tips for TEM and atom-probe analysis. *Micron*, 39(2008): 320-328.
- [13] S.M. Bruemmer, L.E. Thomas. High-resolution analytical electron microscopy characterization of corrosion and cracking at buried interfaces. *Surface and interface analysis*, 31(2001): 571-581.
- [14] Y.S. Lim, H.P. Kim, S.S. Hwang. Microstructural characterization on intergranular stress corrosion cracking of Alloy 600 in PWR primary water environment. *Journal of Nuclear Materials*, 440(2013): 46-54.
- [15] L.E. Thomas, S.M. Bruemmer. High-resolution characterization of intergranular attack and stress corrosion cracking of Alloy 600 in high-temperature primary water. *Corrosion*, 56(2000): 572-587.

- [16] P.M. Scott, M. Le Calver, “Some possible mechanisms of intergranular stress corrosion cracking of alloy 600 in PWR primary water”, In Proceedings of the sixth international symposium on environmental degradation of materials in nuclear power systems-water reactors, (TMS, 1993), 657-665.
- [17] S. Lozano-Perez, J. Dohr, M. Meisnar, K. Kruska. SCC in PWRs: learning from a bottom-up approach. *Metallurgical and Materials Transactions E*, 1(2014): 194-210.
- [18] M. Meisnar, M. Moody, S. Lozano-Perez. Atom probe tomography of stress corrosion crack tips in SUS316 stainless steels. *Corrosion Science*, 98(2015): 661-671.
- [19] S. Lozano-Perez, T. Yamada, T. Terachi, M. Schröder, C. A. English, G. D. W. Smith, C. R. M. Grovenor, B. L. Eyre. Multi-scale characterization of stress corrosion cracking of cold-worked stainless steels and the influence of Cr content. *Acta Materialia*, 57(2009): 5361-5381.
- [20] E.A. West, M.D. McMurtrey, Z. Jiao, G.S. Was. Role of localized deformation in irradiation-assisted stress corrosion cracking initiation. *Metallurgical and Materials Transactions A*, 43(2012): 136-146.
- [21] G.C. Wood, F.H. Stott, D.P. Whittle, Y. Shida, B.D. Bastow. The high-temperature internal oxidation and intergranular oxidation of nickel-chromium alloys. *Corrosion Science*, 23(1983): 9-25.
- [22] D.P. Whittle, Y. Shida, G.C. Wood, F.H. Stott, B.D. Bastow. Enhanced diffusion of oxygen during internal oxidation of nickel-base alloys. *Philosophical Magazine A*, 46(1982): 931-949.
- [23] P.L. Andresen, L.M. Young, P.W. Emigh, R.M. Horn, Stress corrosion crack growth rate behavior of Ni alloys 182 and 600 in high temperature water, in: Proc. of Corrosion 2002, Paper no.2510, NACE, 2002
- [24] T. Shoji, G. Li, J. Kwon, S. Matsushima. Quantification of yield strength effects on IGSCC of austenitic stainless steels in high temperature water, in: Proc. 11th Int. Conf. Environmental Degradation of Materials in Nuclear Power Systems-Water Reactors, Stevenson, August 10–14, 2003.